Acta Metallurgica Sinica (English Letters) (2024) 37:1387–1398
https://doi.org/10.1007/s40195-024-01718-9

Microstructure and Mechanical Properties of the $Ti_{62}Nb_{12}Mo_{12}Ta_{12}W_2$ Refractory High Entropy Alloy Prepared through Spark Plasma Sintering

Zirui Chen[1] · Liyuan Wang[1] · Jiayu Zhao[1] · Guanhua Cui[1] · Zhuo Gao[1] · Zhiyuan Fan[1] · Xiaohui Shi[1] · Junwei Qiao[1]

Received: 24 December 2023 / Revised: 22 February 2024 / Accepted: 26 February 2024 / Published online: 31 May 2024

Abstract
A refractory high entropy alloy $Ti_{62}Nb_{12}Mo_{12}Ta_{12}W_2$ was prepared by mechanical alloying and spark plasma sintering. The microstructure and mechanical properties of the $Ti_{62}Nb_{12}Mo_{12}Ta_{12}W_2$ alloy were analyzed. The experimental results show that the microstructure of the alloy is composed of two BCC phases, an FCC precipitated phase, and the precipitated phase which is a mixture of TiC, TiN and TiO. The alloy exhibits good room temperature compressive properties. The plasticity of the sample sintered at 1550 °C can reach 10.8%, and for the sample sintered at 1600 °C, the yield strength can be up to 2032 MPa, in the meantime the plasticity is 9.4%. The alloy also shows high strength at elevated temperature. The yield strength of the alloy exceeds 420 MPa at 900 °C, and value of which is still above 200 MPa when the test temperature reaches 1000 °C. Finally, the compressive yield strength model at room temperature is constructed. The prediction error of the model ranges from − 7.9% to − 12.4%, expressing fair performance.

Keywords Refractory high-entropy alloy (RHEA) · Mechanical alloying · Mechanical properties · Model · Spark plasma sintering

1 Introduction

High-entropy alloy (HEA) is a new type of alloy with multi-principal elements, which was first proposed by Ye et al. [1] in 2004. HEAs show obviously different characters with traditional alloys due to the complicated chemical compositions. Four basic laws of HEAs were found and summarized, namely, the high entropy effect in thermodynamics [2], the "cocktail" effect in performance [3], the hysteresis diffusion effect in dynamics [4] and the lattice distortion effect in structure [5].

The characters of HEAs bring excellent mechanical properties, such as excellent strength, favorable hardness, superior wear resistance and amazing corrosion resistance. Therefore, HEAs exhibit broad research value and application prospects [6, 7]. In recent years, a mass of research work has been carried out on HEAs [4–15]. For example, Cantor et al. developed a single-phase FCC structure alloy [16]. Chen et al. [17] designed a $Cu_{0.5}$NiAlCoCrFeSi HEA with a small amount of nano-amorphous phase dispersed between dendrites. Wu et al. [18] found that for Al_xCoCrCuFeNi alloys, as the Al content increases, the main composition phase of the alloy will change from FCC to BCC. Above studies mainly focus on HEA systems containing 3*d* transition group elements, such as the alloy FeCrNiCoMn [16].

Refractory HEA (RHEA) is a special branch of the large family of HEA, for which elements with high melting point of the IV, V and VI subgroups (such as Mo, V, Nb, Ta, W) usually serve as main elements. RHEAs generally have a single BCC structure. However, under many circumstances, a small volume of intermetallic compounds (B2 phase), FCC phase, HCP phase, silicide and carbide are contained. Compared with the FCC-structured HEAs (for example, the CoCrFeMnNi series), RHEAs (such as NbMoTaW [8], HfNbTiZr [10], AlCrNbTiV [11] and NbTaTiV [19]) exhibit the advantages of excellent strength and fair hardness at room temperature, at the same time, maintain thermal stability at high temperatures. These advantages make RHEAs great

Available online at http://link.springer.com/journal/40195

✉ Xiaohui Shi
sxhtough@126.com

[1] College of Materials Science and Engineering, Taiyuan University of Technology, Taiyuan 030024, China

candidate hot-end component materials in the fields of aerospace, military equipment and nuclear industry.

However, the shortcomings of RHEAs are also obvious. Firstly, their room-temperature plasticity is generally poor. Currently, only a small part of RHEAs such as HfNbTaTiZr developed by Senkov et al. [9] shows acceptable tensile plasticity. After 86.4% cold deformation, followed by heat treatment at 1000 °C for 2 h, the elongation can reach 9.7%. Secondly, the densities of RHEAs are always high due to the high-density elements in structure. The two shortcomings severely restrict the application of RHEAs. Studies have shown that the addition of light element Ti can not only reduce the density of RHEA, but also improve its mechanical properties. By preparing two RHEAs, MoNbTaW and MoNbTaTi, Han [12] found that the yield strength at room temperature increased by 33% after adding the Ti element, at the expense of slight decrease in hardness and fracture toughness.

At present, bulk RHEAs are mostly prepared by vacuum arc melting method [7–9, 12, 19]. By contrast, the powder metallurgy method has a series of advantages such as short preparation temperature, uniform mixing of material components, near-net formation, and dramatic properties [12–15]. However, the reports on the preparation of RHEAs by the powder metallurgy method are limited. Kang et al. [13] prepared a single-phase BCC structure WNbMoTaV alloy using powder metallurgy technology. By comparing with the alloy obtained through vacuum arc melting method, it exhibits excellent mechanical properties. The compressive yield strength is 2612 MPa, which is higher than the twice strength of the same alloy cast by vacuum arc melting method (1246 MPa). Long et al. [14] sintered the WNbMoTaVCr alloy at 1773 K using spark plasma sintering system. The alloy has an average grain size of 1.24 μm, and the compressive strength at room temperature can reach 3416 MPa.

To sum up, the addition of Ti in RHEA and the change of preparation method from vacuum arc melting to powder metallurgy technology are favorable to remedy the shortcomings of RHEA. In this paper, a Ti–rich $Ti_{62}Nb_{12}Mo_{12}Ta_{12}W_2$ RHEA was prepared by powder metallurgy method (including mechanical alloying, namely, MA, and spark plasma sintering, namely SPS). The effects of sintering temperature on its microstructure and mechanical properties were studied. Moreover, a compressive yield strength model was established and verified.

2 Experimental

The RHEA powders with nominal composition of $Ti_{62}Nb_{12}Mo_{12}Ta_{12}W_2$ (atom ratio) were prepared using MA method. The MA process was carried out using the planetary ball mill (MSK-SFM-I). High-purity (≥ 99.9 wt%) Ti (< 100 μm), Nb (< 100 μm), Mo (< 1 μm), Ta (< 5 μm) and W (< 1 μm) powders and the stainless-steel grinding ball were mixed and sealed in a stainless-steel grinding tank in a weight ratio of 10:1. The rotation speed was set as 300 r/min. The running time of a single round is 30 min, and an interval of 15 min was added between two adjacent rounds. The total effective milling time is 50 h, and the alloyed RHEA powder after milling was collected. To prevent the oxidation of powder, powder loading and extraction processes were completed in Argon atmosphere.

Then, the alloyed powder was loaded into a high-strength graphite mold with an inner diameter of 20 mm and held at 1550–1700 °C for 10 min under an axial pressure of 50 MPa. The sintering process was conducted using SPS-20T-10-III system (Shanghai Chenhua Technology Co., Ltd). After sintering, the bulk samples were furnace-cooled to 100 °C and then removed (a thin graphite foil existed between the sample and the graphite mold which facilitates the demolding) after unloading. The density of the alloy was measured using the Archimedes method. Each sample was measured five times, and the average value was taken.

The phases of the sintered samples were identified by X-ray diffraction (XRD, PANalytical AERIS) with Cu $K\alpha$ radiation. The microstructures were characterized using a scanning electron microscope (SEM, Phenom XL). The element distributions were also analyzed by an energy-dispersive spectrometer (EDS) equipped on the SEM. The average grain size of the sintered alloy and the size of needle-like precipitates were estimated by ImageJ analysis software.

The hardness values of different phase regions of samples sintered at different temperatures were measured using vickers hardness tester (MH-600). The compressive properties at room temperature were tested employing a universal mechanical testing machine (Instron 5969). The samples had a cylindrical shape of around Φ 3 × 4.5 mm, and the engineering strain rate was set as 1×10^{-3} s^{-1}. After compression, the fracture morphology was observed by SEM. The high-temperature compression tests at 900 °C and 1000 °C were carried out embracing Gleeble 3800 thermo-force simulation system. The cylindrical samples with the dimensions of around Φ 6 × 9 mm were adopted. The true strain rate was set as 1×10^{-3} s^{-1}. The samples after high-temperature compression were cut along the load direction, and the microstructures of the section faces were characterized using SEM.

3 Results and Discussion

$Ti_{62}Nb_{12}Mo_{12}Ta_{12}W_2$ alloy with fine grain size and uniform microstructure was successfully prepared by MA + SPS. Compared with RHEAs, the content of light element Ti of the $Ti_{62}Nb_{12}Mo_{12}Ta_{12}W_2$ alloy is higher, so the density of

the corresponding alloy is relatively low. The theoretical density of the alloy can be calculated as follows [20]:

$$\rho_{\text{cacl}} = \frac{100}{\sum_{i=1}^{N}\left(\omega_i/\rho_i\right)}. \tag{1}$$

$$\omega_i = \frac{c_i M_i}{\sum_{i=1}^{N} c_i M_i}. \tag{2}$$

where ω_i is the mass percentage of the ith component. ρ_i and ω_i are the density and mass fraction of the ith component, respectively. All of them are listed in Table 1. The theoretical density of the HEA is evaluated as 7.404 g/cm^3, which is lower than that of many traditional super alloys and RHEAs [21–28], as shown in Fig. 1. The average density of the alloy measured actually is in the range from 7.012 to 7.315 g/cm^3.

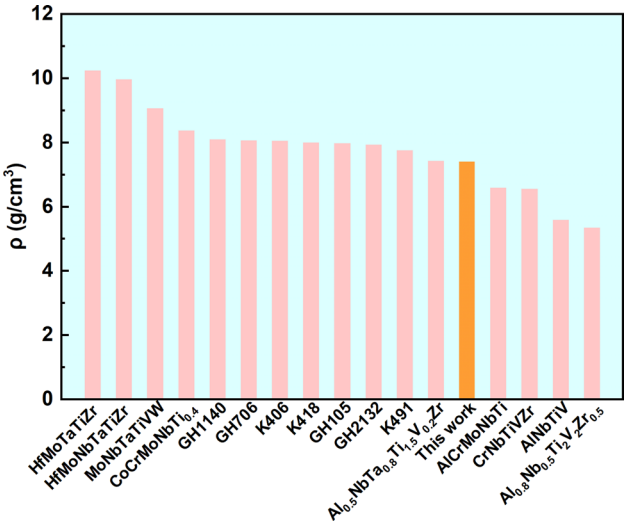

Fig. 1 Comparison of the density of $Ti_{62}Nb_{12}Mo_{12}Ta_{12}W_2$ with some typical superalloys and RHEAs

3.1 Phase Formation Mechanism Analysis

Based on the Hume-Rothery law [29] and some basic parameters of the components, researchers have summarized and proposed some empirical parameters to predict the phase formation and structural stability of HEA. Based on the comprehensive analysis of these parameters, the alloy $Ti_{62}Nb_{12}Mo_{12}Ta_{12}W_2$ was designed. Zhang et al. [30] proposed two parameters to predict the formation of solid solution by mixing enthalpy (ΔH_{mix}) and atomic size difference (δ_r), as follows:

$$\Delta H_{\text{mix}} = \sum_{i=1, i\neq j}^{N} 4\Delta H_{AB}^{\text{mix}} c_i c_j. \tag{3}$$

$$\delta_r = 100\% \times \sqrt{\sum_{i=1}^{n} c_i\left(1 - r_i/\bar{r}\right)^2}. \tag{4}$$

$$\bar{r} = \sum_{i=1}^{n} c_i r_i. \tag{5}$$

where $\Delta H_{AB}^{\text{mix}}$ is the enthalpy of mixing elements A and B, c_i and c_j are the atomic percentages of elements i and j, respectively. Parameter r_i refers to the atomic radius of the ith component, and $\bar{r}$ is the average atomic radius of all constituent elements, which can be calculated according to the rule of mixtures. ΔH_{mix} represents the mixing enthalpy of the alloy, which measures the possibility of forming stable intermetallic compounds. The basic parameters of the Ti, Nb, Mo, Ta, W elements studied in present work are listed in Table 1. The mixing enthalpy of atomic pairs of Ti, Nb, Mo, Ta, W are shown in Table 2 [31]. The ΔH_{mix} of the $Ti_{62}Nb_{12}Mo_{12}Ta_{12}W_2$ was calculated to be − 1.372 kJ/mol.

δ_r represents the degree of atomic size mismatch, which will lead to local elastic deformation affecting the topological instability of the alloy system [32]. The value of δ_r is calculated to be 2.094%. According to Zhang et al. [30], when $\delta_r < 6.6\%$ and -15 kJ/mol $< \Delta H_{\text{mix}} < 5$ kJ/mol, the HEA tends to form a simple solid solution after rapid solidification. Comparing the calculated results with the standard parameters, it is considered that $Ti_{62}Nb_{12}Mo_{12}Ta_{12}W_2$ RHEA can form a simple solid solution.

Table 1 Basic parameters of the constituent elements of $Ti_{62}Nb_{12}Mo_{12}Ta_{12}W_2$

Element	r (nm)	T_m (K)	VEC	M (g/mol)	ρ (g/cm^3)
Ti	0.145	1941	4	47.87	4.51
Nb	0.143	2741	5	92.91	8.57
Mo	0.136	2896	6	95.94	10.23
Ta	0.143	3290	5	180.95	16.68
W	0.137	3695	6	183.84	19.35

Table 2 Mixing enthalpy of atomic pairs of $Ti_{62}Nb_{12}Mo_{12}Ta_{12}W_2$ [20] (kJ/mol)

Element	Ti	Nb	Mo	Ta	W
Ti	0	2	−4	1	−6
Nb		0	−6	0	−8
Mo			0	−5	0
Ta				0	−7
W					0

In order to further improve the formation criterion of HEA solid solution, Yang et al. [33] proposed the thermodynamic parameter Ω in subsequent research to evaluate the formation ability of the HEA solid solution, as shown below:

$$\Omega = T_m \Delta S_{mix} / \left| \Delta H_{mix} \right|. \tag{6}$$

$$T_m = \sum_{i=1}^{n} c_i \left(T_m \right)_i. \tag{7}$$

$$\Delta S_{mix} = -R \sum_{i=1}^{N} c_i \ln c_i. \tag{8}$$

where T_m means the average melting point of the alloy system, which can be calculated according to the rule of mixtures. $(T_m)_i$ refers to the melting point of the ith component element, and $R = 8.314$ J/(mol K) is the gas constant. Ω represents the ratio of the contribution of enthalpy and entropy of the system at the melting point temperature. According to statistics, when $\delta_r < 6.6\%$ and $\Omega \geq 1.1$, the mixed entropy dominates the formation of a simple solid solution phase in the alloy [33]. In contrast, the formation of the solid solution phase is inhibited, and the intermetallic compound or segregation is preferentially formed. According to the formula, the calculated value of Ω is 16.185, together with $\delta_r = 2.094\%$, indicates that the $Ti_{62}Nb_{12}Mo_{12}Ta_{12}W_2$ alloy tends to form a solid solution phase without intermetallic compounds.

According to the parameters above, it can be comprehensively judged that $Ti_{62}Nb_{12}Mo_{12}Ta_{12}W_2$ alloy could form a solid solution phase, but the specific type of the solid solution phase cannot be determined by above criteria.

Guo et al. [34] proposed that for multicomponent HEAs, the valence electron concentration (VEC) can be used to describe the stability of the FCC phase and the BCC phase, which can be calculated as follows:

$$\mathrm{VEC} = \sum_{i=1}^{N} c_i (\mathrm{VEC})_i. \tag{9}$$

where $(\mathrm{VEC})_i$ is the VEC of the ith element. By studying the relationship between valence electron concentration and solid solution phase composition, the formation law of solid solution phase in HEAs was found: The FCC phase is stable at higher VEC, whereas the BCC phase is stable at lower VEC. Quantitative criteria: The BCC phase forms when $\mathrm{VEC} \leq 6.87$, FCC + BCC dual phase or even multiphase structure is formed when $6.87 < \mathrm{VEC} < 8$, and the FCC phase appears when $\mathrm{VEC} \geq 8$. As calculated, the VEC of the $Ti_{62}Nb_{12}Mo_{12}Ta_{12}W_2$ alloy is 4.52, which is less than 6.87, so the solid solution formed by the alloy is most possibly BCC phase.

Table 3 Phase formation parameters of $Ti_{62}Nb_{12}Mo_{12}Ta_{12}W_2$

ΔS_{mix} (J/K·mol)	ΔH_{mix} (kJ/mol)	δ (%)	Ω	VEC
9.461	− 1.372	2.094	16.185	4.52

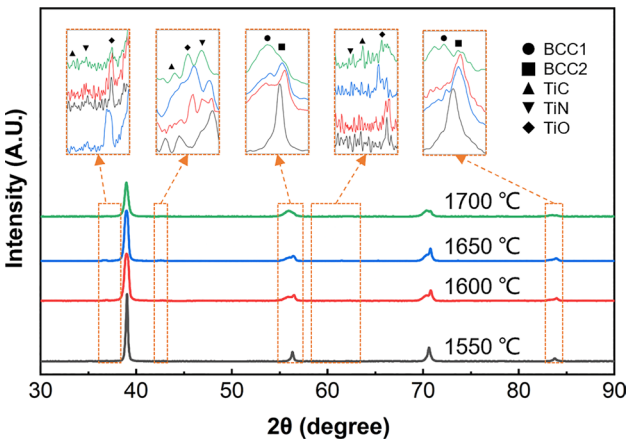

Fig. 2 X-ray diffraction (XRD) patterns of $Ti_{62}Nb_{12}Mo_{12}Ta_{12}W_2$ sintered at different temperatures

In summary, considering several parameters listed in Table 3, the simple solid solution with BCC structure tends to be obtained for $Ti_{62}Nb_{12}Mo_{12}Ta_{12}W_2$ RHEA, but the formation possibility of other phases is not ruled out. This can be explained in this way: it should be noted that above criterion is summarized from RHEAs prepared by the melting method. Considering the possibility of the introduction of impurity elements (such as C, N and O) into the system during MA and SPS process, the phase formation law mentioned above may appear prediction deviation.

3.2 Microstructure Analysis

The X-ray diffraction patterns of $Ti_{62}Nb_{12}Mo_{12}Ta_{12}W_2$ sintered at different temperatures are shown in Fig. 2. It can be seen that the sintered bulk RHEA is composed of BCC and FCC phases. In particular, the diffraction peak morphology of the BCC phase changes with increasing sintering temperature. The formed matrix phase is defined as BCC1 phase. For the sample sintered at 1550 °C, BCC phase appears single diffraction peak. In this situation, the single BCC phase is named as BCC2. As the sintering temperature raises, the BCC1 phase which has slightly different lattice constant with the BCC2 phase gradually increases, thus the diffraction peak of BCC phase becomes bifurcate.

After grinding, polishing and etching, the alloy sintered at different temperatures showed similar structures, including

four morphologies: equiaxed grain structure, lamellar structure, bright parts and black patches. The microstructure of sample sintered at 1550 °C shown in Fig. 3 is taken as an example. The backscattered electron (BSE) diagrams and the corresponding EDS maps of $Ti_{62}Nb_{12}Mo_{12}Ta_{12}W_2$ sintered at different temperatures are shown in Fig. 4.

The matrix of the alloy appears as equiaxed grains (namely BCC1). The Ti element is enriched at the grain boundary. There are lamellar structures inside the grains. Their element distribution is relatively uniform and shows little difference with matrix. Therefore, they are still deemed as the matrix phase.

There are black patches with an unfixed size and shape at the grain boundary, which are rich in Ti. This is due to that phases rich in light atoms have dark contrast under BSE. It is speculated that a large amount of Ti element is not dissolved into the high entropy phase. Because the lattice constant is close to the matrix, it is still belonging to the BCC1 phase and not shown as a new phase in the XRD pattern. The size and the volume fraction of the black block in the sample

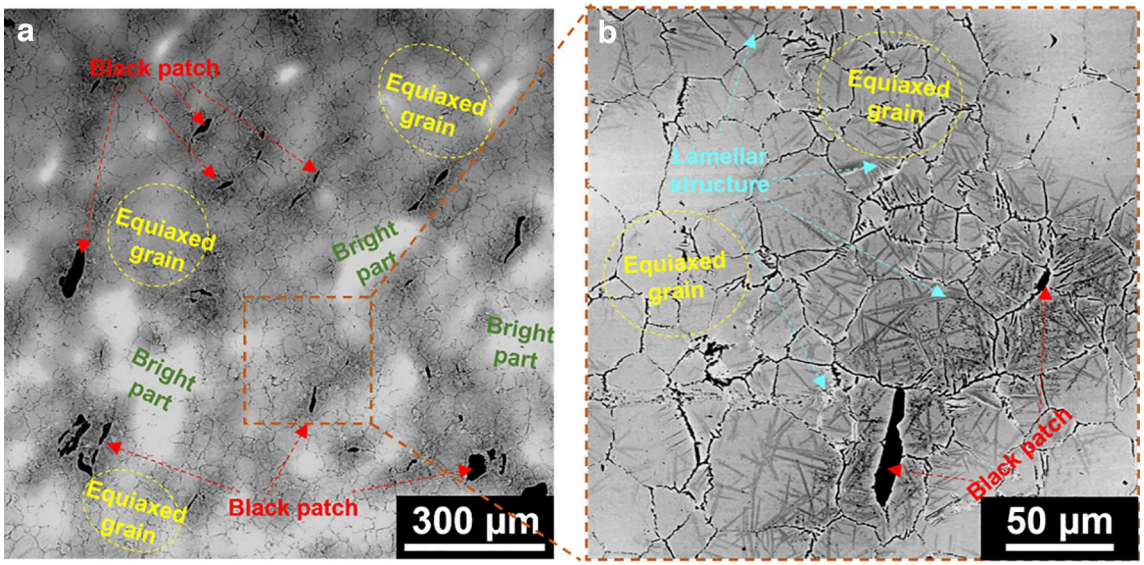

Fig. 3 SEM-BSE of $Ti_{62}Nb_{12}Mo_{12}Ta_{12}W_2$ sintered at 1550 °C **a**, local details of the inner part of the brown wire frame **b**

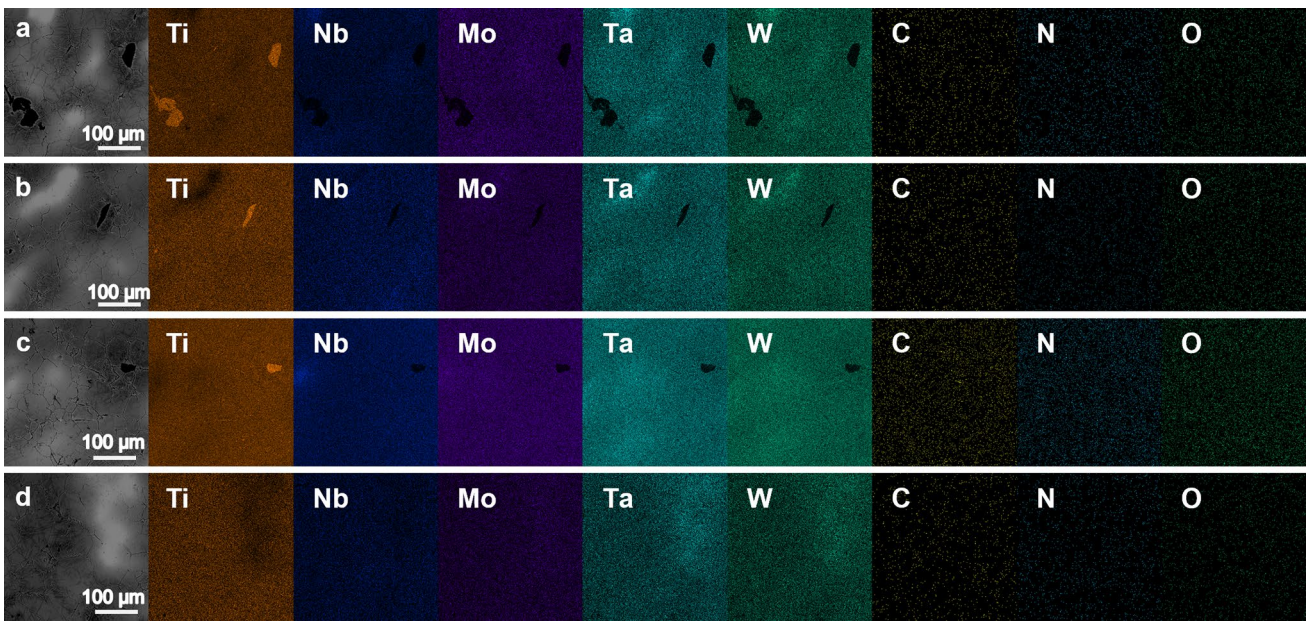

Fig. 4 SEM-BSE and EDS patterns of $Ti_{62}Nb_{12}Mo_{12}Ta_{12}W_2$ sintered at 1550 °C **a**,1600 °C **b**,1650 °C **c**,1700 °C **d**

sintered at 1550 °C is large, and become smaller for the other three, which can be intuitively found in Fig. 4. This is because that the Ti element would gradually dissolve into matrix with increasing sintering temperature.

The bright part in microstructure is poor in Ti, while the Nb, Ta and W elements are enriched. With the increase in sintering temperature, the enrichment degree of the four elements decreases and gradually distributes uniformly in the order of Mo, Nb, Ta and W, corresponding to the BCC2 phase in the XRD pattern. As the sintering temperature reaches 1700 °C, Mo and Nb are dissolved into the matrix completely, and Ta and W are still not completely dissolved.

According to the EDS results, BCC1 phase is mainly composed of Ti, Mo, Ta, Nb and W, while the BCC2 phase is mainly composed of Mo, Ta, Nb and W. When sintered at 1550 °C, only a small part of Mo, Ta, Nb and W atoms had been dissolved, while most tend to form BCC2 phase by solid solution with each other rather than BCC1 phase by solid solution with Ti. The volume fraction of the BCC1 phase formed is low and the difference between BCC1 phase and BCC2 phase is small, so it cannot be clearly observed in the XRD pattern, while the peak intensity is particularly high, due to the superposition of the two-phase diffraction peaks. As the sintering temperature increases, the BCC1 phase continuously forms and Mo, Ta, Nb and W gradually dissolved into it. For the sample sintered at 1700 °C, the diffraction peak intensity of the BCC1 phase is slightly higher than that of the BCC2 phase, indicating that more Mo, Ta, Nb and W elements are dissolved into the high-entropy phase. It is speculated that Mo, Ta, Nb and W will be completely dissolved into the matrix to form a single high-entropy BCC phase as the sintering temperature continues to increase. Besides the BCC phase, there is a small amount of FCC phase formed in the $Ti_{62}Nb_{12}Mo_{12}Ta_{12}W_2$ RHEA, which is small in size and cannot be recognized in the EDS maps. The lattice constants of the FCC phase are calculated to be between 0.421 and 0.423 nm from the crystal plane index *h, k, l* and the corresponding interplanar spacing *d* according to the following formula: $a = d\sqrt{h^2 + k^2 + l^2}$, which is close to the lattice constants of TiC, TiO and TiN, as listed in Table 4. In addition, C, N and O can be introduced into the alloy during ball milling and sintering. Therefore, it is speculated that the FCC phase is a mixture of TiC, TiO and TiN marked in the XRD pattern as shown in Fig. 2, which can produce some strengthening effect to the matrix.

Table 4 Lattice constant of TiC, TiO, TiN [13] and the FCC phase in $Ti_{62}Nb_{12}Mo_{12}Ta_{12}W_2$

	Lattice constant (nm)
TiC	0.433
TiN	0.424
TiO	0.418
1550 °C	0.422
1600 °C	0.423
1650 °C	0.422
1700 °C	0.421

3.3 Mechanical Property

The micro-Vickers hardness of different phases for the samples sintered at different temperatures was measured under a load of 300 g. During the tests, the dwell time of each load is 15 s. The Vickers hardness results and the corresponding error ranges are shown in Fig. 5. It can be found that for samples sintered at 1550 °C, 1600 °C, 1650 °C and 1700 °C, the average hardness of BCC1 phase is 619 HV, 591 HV, 553 HV and 514 HV, respectively, while the average hardness of BCC2 phase is 552 HV, 549 HV, 529 HV and 479 HV, respectively. As the sintering temperature increases, the average hardness of both BCC1 phase and BCC2 phase continues to decrease. On the whole, the hardness of BCC1 phase is higher than that of BCC2 phase, which is speculated to be due to the higher number of element types with different atomic size and modulus in BCC1 phase. The higher mismatch of atomic size and modulus, the stronger effect of solution strengthening.

By subtracting the stiffness of the testing machine and the mold, the corrected compressive engineering stress–strain curves are shown in Fig. 6. It can be found that the plasticity of the sample sintered at 1550 °C is the best, which can reach 10.8% ± 0.9%. By increasing the sintering temperature to 1600 °C, the yield strength increases to 2030 ± 2 MPa, combined with not bad plasticity (9.4% ± 0.3%). As the sintering temperature continues to increase, the yield strength and plasticity tend to decrease, as listed in Table 5. This

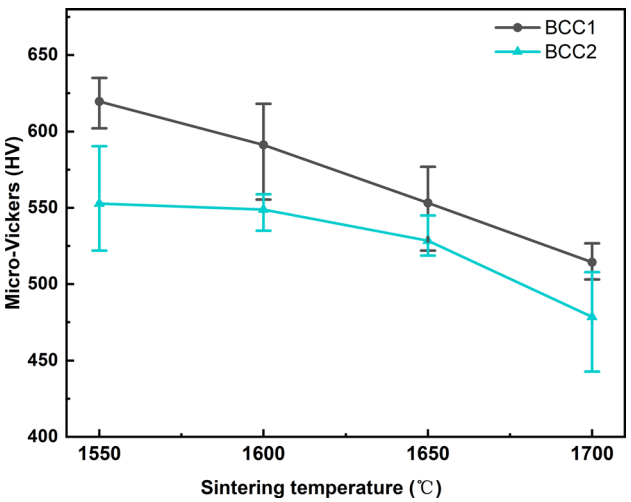

Fig. 5 Hardness values of different phase regions of samples sintered at different temperatures

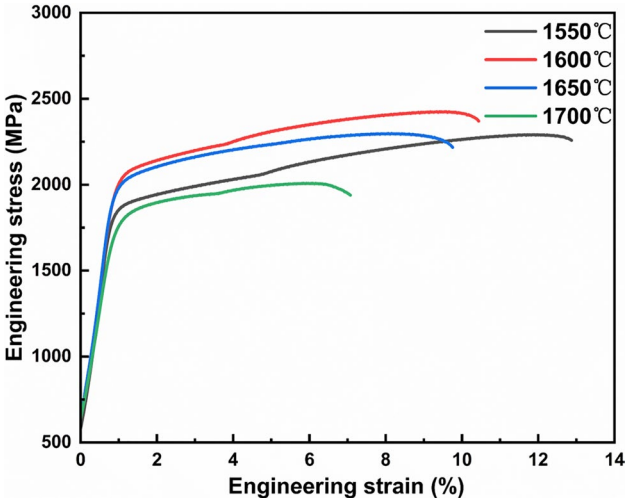

Fig. 6 Engineering stress–strain curves of $Ti_{62}Nb_{12}Mo_{12}Ta_{12}W_2$ sintered at different temperatures

Table 5 Compression properties of the $Ti_{62}Nb_{12}Mo_{12}Ta_{12}W_2$ alloy at room temperature

Sintering temperature (°C)	Yield strength (MPa)	Peak strength (MPa)	Plasticity (%)
1550	1843	2425	11.7
1600	2032	2290	9.1
1650	1995	2297	8.7
1700	1685	2007	5.8

results from the changes of the relative content and hardness of BCC1 phase and BCC2 phase as shown in Fig. 5. Compared with the NbMoTaW alloy prepared by vacuum arc melting [8], the strength and plasticity of the samples are higher, indicating that the powder metallurgy method is superior in the preparation of refractory high-entropy alloy. Meanwhile, the higher plasticity than that of the sintered WNbMoTaV [13] may indicate that the addition of Ti could optimize plasticity.

The surface morphologies of the fractured compressive specimens are shown in Fig. 7. It can be found that the main crack propagates along the load direction and deflects slightly (Fig. 7a–d). There are small "X"-shaped secondary cracks on the side surface, and some slip deformation bands can also be found near the crack (Fig. 7e–h). There is no comminuted fracture or shear fracture in the cylindrical sample during compression. On the whole, the longitudinal main cracks along the stress direction divide the sample into two or more columnar parts. This phenomenon often occurs in the compression process of brittle materials such as engineering ceramics and cement or in the process of metal rolling, which is related to the formation of additional stress inside the compressed sample, resulting in uneven stress. After the main crack appears, the unstable deformation occurs. When the pressure continues to increase, the compressive specimens eventually undergo a transverse fracture or fragmentation [12]. According to the fracture surface in Fig. 7, the morphology of river pattern was found, some rock candy-like pattern was also found. This indicates that it is a mixed fracture mode with transgranular fracture and intergranular fracture simultaneously (Fig. 7i–l)

The thermal simulation compression test at elevated temperatures was carried out. It is worth mentioning that the true plasticity of the specimen is not really touched due to the automatic unloading when the true strain reaches 0.5 during compression, and all the specimens are obviously upset and no cracking occurs. Figure 8 shows the true stress–strain curves of samples compressed at elevated temperatures. By analyzing these curves, it can be found that the strength of the RHEA decreases as the test temperature increases. Obvious softening stage occurs after reaching the peak stress. This is because after the start of the test, due to the dislocation proliferation, the dislocation density increases, and the work hardening phenomenon occurs. After that, it enters the stage of uniform deformation. Due to the thermal activation conditions provided by high temperature, the dynamic recovery phenomenon appears which offsets the work hardening. The proliferation of dislocations is less than the disappearance, and the softening is obvious, which shows continuous stress reduction in the stress–strain curve.

When compressed at 900 °C, softening is obvious after reaching peak stress. The yield strength of the samples sintered at 1600 °C and 1650 °C are almost the same (428 MPa and 426 MPa, respectively). Specially, for the sample sintered at 1700 °C, the yield strength significantly increased to 493 MPa. According to Fig. 2, the relative content of the BCC1 phase increases when the sintering temperature rises to 1700 °C. Accordingly, the content of the needle-like structure of BCC1 phase may also increase. Needle-like structure gets good ability to impede dislocation movements. Therefore, the overall yield strength of the sample sintered at 1700 °C is significantly higher than that of the samples sintered at 1600 °C and 1650 °C.

When compressed at 1000 °C, the yield strength of the sample continuously decreases with increasing sintering temperature (280 MPa, 253 MPa, and 212 MPa, respectively. Table 6).

At 1000 °C, the samples were compressed to the true strain of 50% without cracks. This indicates that the plasticity of $Ti_{62}Nb_{12}Mo_{12}Ta_{12}W_2$ alloy at high temperature is excellent, which further reflects the enhancement effect of Ti element on the properties of the alloy.

The compressed samples are cut along the loading direction, these sections were ground, polished, and then corroded, the morphologies are shown in Fig. 9.

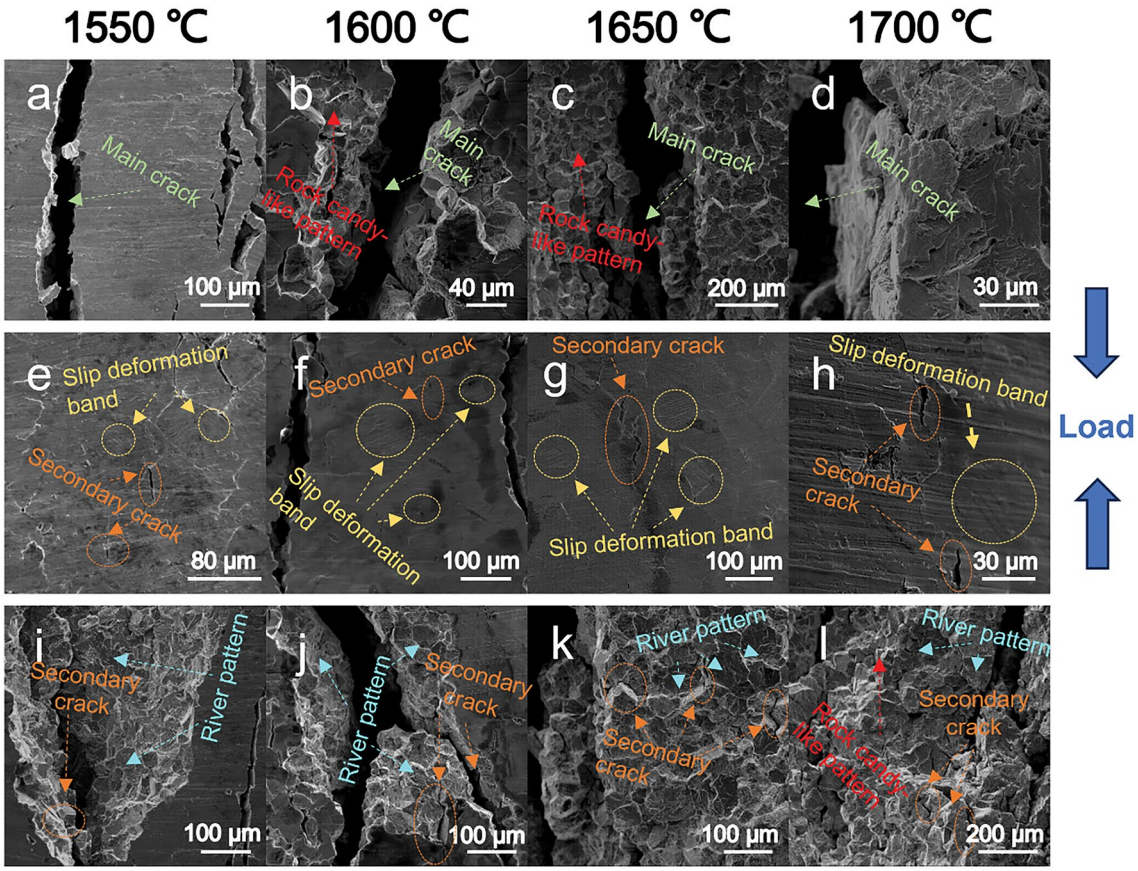

Fig. 7 Morphologies of $T_2Nb_{12}Mo_{12}Ta_{12}W_2$ sintered at 1550 °C **a**, **e**, **i**, 1600 °C **b**, **f**, **j**, 1650 °C **c**, **g**, **k**, 1700 °C **d**, **h**, **l** after compression at room temperature: main crack **a**–**d**, side surface **e**–**h**, fracture surface **i**–**l**

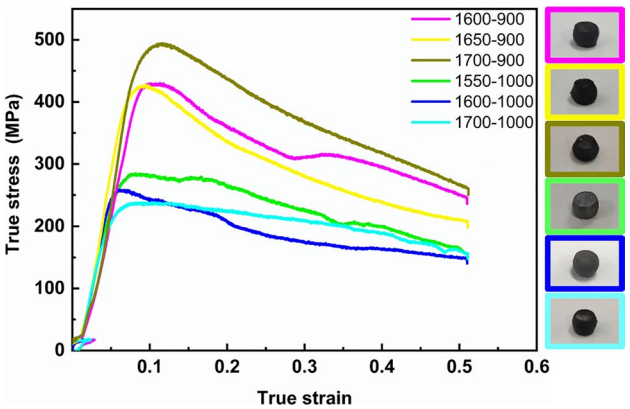

Fig. 8 True stress–strain curves of $Ti_{62}Nb_{12}Mo_{12}Ta_{12}W_2$ RHEA compressed at elevated temperatures and the corresponding macroscopic shape of the samples after compression. The legend indicates the sintering temperature (1550 °C, 1600 °C, 1650 °C, 1700 °C) and test temperature (900 °C, 1000 °C)

Combined with Figs. 3 and 9, it can be found that the grains of the samples after high temperature compression are obviously flattened and elongated, and the central part of the samples is seriously deformed. After high temperature compression, the number and the size of the black patches were significantly reduced, the BCC1 phase (equiaxed grains) was increased, and the BCC2 phase (bright part) was reduced, indicating that under high temperature conditions, the atoms were diffused, the elements were further dissolved, as a result, their distribution was more uniform.

Table 6 Compression properties of the $Ti_{62}Nb_{12}Mo_{12}Ta_{12}W_2$ alloy at elevated temperatures

Sintering temperature (°C)	Test temperature (°C)	Yield strength (MPa)
1600	900	374
1650	900	370
1700	900	423
1550	1000	251
1600	1000	227
1700	1000	197

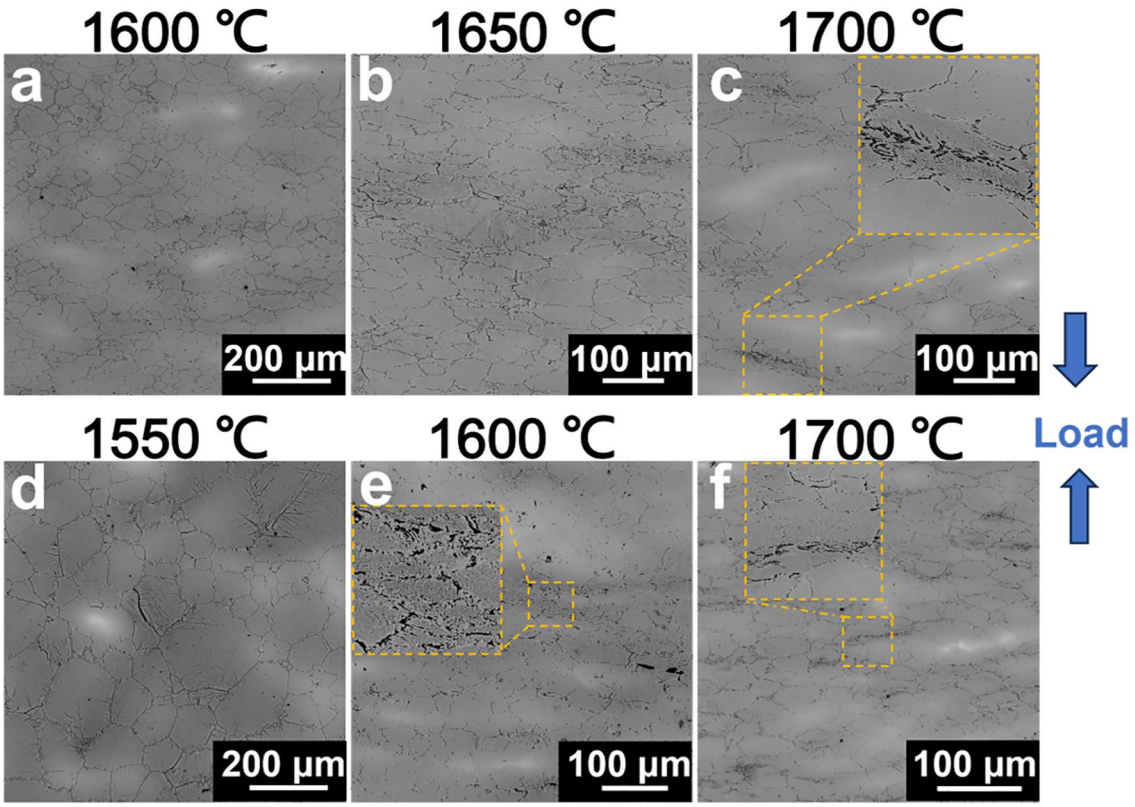

Fig. 9 Metallography of the sample section after compression at 900 °C **a–c** and 1000 °C **d–f**

3.4 Strengthening Model

There are many factors that contribute to the yield strength. According to previous research [14], the compressive yield strength of the alloy can be expressed as follows:

$$\sigma_y = \sigma_0 + \Delta\sigma_{ss} + \Delta\sigma_{gb} + \Delta\sigma_{dis} + \Delta\sigma_{or}. \quad (10)$$

where σ_0 means the intrinsic yield strength, $\Delta\sigma_{ss}$, $\Delta\sigma_{gb}$, $\Delta\sigma_{dis}$ and $\Delta\sigma_{or}$ are the contributions of solid solution, grain boundary, dislocation and precipitation to the yield strength, respectively.

The intrinsic yield strength σ_0 of this alloy is calculated using the yield strength of annealed metal Ti, Nb, Mo, Ta and W according to the following formula [35]:

$$\sigma_0 = \sum c_i \sigma_{iy} \quad (11)$$

where c_i represents the atomic percentage of the ith element in the alloy, σ_{iy} refers to the yield strength of the annealed metal element of the ith element listed in Table 7. The intrinsic yield strength of $Ti_{62}Nb_{12}Mo_{12}Ta_{12}W_2$ is calculated to be 188 MPa.

For $Ti_{62}Nb_{12}Mo_{12}Ta_{12}W_2$ alloy, the solid solution strengthening effect plays a very important role in the contribution of strength. It is made up of substitutional solid solution strengthening and interstitial solid solution strengthening as follows:

$$\Delta\sigma_{ss} = \Delta\sigma_{sss} + \Delta\sigma_{iss}. \quad (12)$$

where $\Delta\sigma_{sss}$ and $\Delta\sigma_{iss}$ are substitutional solid solution strength and interstitial solid solution strength, respectively.

Due to the generation of a simple solid solution phase, a large number of solute atoms gather around the dislocations, which hinders the movement of the dislocations [36]. In the HEA system, all the constituent elements can be considered as principal elements, and thus each principal element atom can be regarded as a solute atom, and the dilute solution solid solution strengthening model of the classical alloy is no longer applicable to the high-entropy alloy system. Therefore, Senkov et al. [9] constructed a high-entropy replacement solid solution strengthening model based on Labusch solid solution strengthening theory in 2011, as shown below:

$$\Delta\sigma_{sss} = \left(\sum \left(\Delta\sigma_i\right)^{3/2}\right)^{2/3}. \quad (13)$$

where $\Delta\sigma_i$ is the solid solution strengthening value of the ith component element, which can be calculated using the following formula:

Table 7 Related parameters of the strength model

Parameter	σ_{iy} (MPa)	G_i (GPa)	r_i (nm)	K_y (MPa μm$^{1/2}$)
Ti	140 [35]	45.6	0.145	190 [39]
Nb	207 [35]	37.5	0.143	340 [39]
Mo	345 [35]	125.6	0.136	630 [39]
Ta	165	69	0.143	760 [39]
W	750 [35]	160.6	0.137	1000 [39]

$$\Delta\sigma_i = AG\delta_i^{4/3}c_i^{2/3}. \tag{14}$$

$$G = \sum c_i G_i. \tag{15}$$

where A is the material constant, which is 0.04 for RHEAs. G refers to the shear modulus. G_i means the shear modulus of the ith element listed in Table 7. c_i represents the atomic percentage content of the ith component element. G is calculated to be 59.336 GPa according to the mixture rule. δ_i means the atomic mismatch of the ith component, which includes the atomic size mismatch and the shear modulus mismatch. The specific calculation formula of δ_i is as follows:

$$\delta_i = \delta_{iG} + \beta\delta_{ir}. \tag{16}$$

where β is a constant depending on the type of movable dislocation. For the BCC RHEA with screw dislocation, the value of β is 2. δ_{iG} represents the mismatch of the shear modulus, which represents the gap of the element shear modulus. δ_{ir} refers to the mismatch of atomic size, which represents the difference of atomic size. They can be calculated by the following formulas:

$$\delta_{ir} = \frac{9}{8}\sum c_j \cdot r_{ij}. \tag{17}$$

$$r_{ij} = \frac{2\left(r_i - r_j\right)}{r_i + r_j}. \tag{18}$$

$$\delta_{iG} = \frac{9}{8}\sum c_j \cdot G_{ij}. \tag{19}$$

$$G_{ij} = \frac{2\left(G_i - G_j\right)}{G_i + G_j}. \tag{20}$$

where G_{ij} is the difference in shear modulus between the ith element and the jth element; r_{ij} is the difference in atomic radius between element i and element j. The related parameters are shown in Table 7, and the calculated substitutional solid solution strength $\Delta\sigma_{sss}$ is 908 MPa.

RHEAs prepared by the MA + SPS method usually contain more impurity elements such as C, N and O. Impurity elements exist in the matrix phase in the form of interstitial atoms. Thus, the interstitial solid solution strengthening effect of this alloy needs to be considered. The expression of the interstitial solid solution strengthening model in refractory high-entropy alloys is as follows [37]:

$$\Delta\sigma_{iss} = Qc_m^{1/2} = M\gamma Gc_m^{1/2}. \tag{21}$$

where Q represents the material constant of the alloy. M is the Taylor factor. Studies have shown that in some BCC alloys, the Taylor factor is taken as 2.9 [14]. γ is the proportional constant, which is taken 1 in present work. G refers to the shear modulus of alloy, and c_m is the percentage content of interstitial solid solution atoms in the alloy matrix which is set as the sum of the content of the C, N and O atoms obtained from the EDS results. For the samples sintered at 1550 °C, 1600 °C, 1650 °C and 1700 °C, the c_m values are 2.9%, 3.77%, 4.42% and 3.55%, respectively. Finally, $\Delta\sigma_{iss}$ are calculated to be 29 MPa, 33 MPa, 36 MPa and 32 MPa, respectively.

Grain boundary strengthening effect $\Delta\sigma_{gb}$ means that by reducing the grain size of the alloy, the superficial area of grain boundaries can increase, so the slip of dislocations is limited to the narrower grains and plugged at the grain boundaries and then increases the slip resistance of the dislocations. Macroscopically, the yield strength of the material is improved. The grain boundary strengthening effect can be calculated according to the Hall–Petch relationship [38]:

$$\Delta\sigma_{gb} = k_y D^{-1/2}. \tag{22}$$

where k_y is the Hall–Petch coefficient listed in Table 7 [39], which is used to measure the pinning constant of the contribution of the grain boundary strengthening, and D refers to the average grain size. The k_y of the BCC structure is much higher than that of the FCC or HCP structure. The Hall–Petch coefficient of $Ti_{62}Nb_{12}Mo_{12}Ta_{12}W_2$ RHEA is calculated to be 345 MPa μm$^{1/2}$ based on the Hall–Petch coefficient of pure Ti, Nb, Mo, Ta and W and the atomic ratio of each element in the material using the formula: $k_y = \sum c_i k_{iy}$. The average grain sizes of the samples sintered at 1550 °C, 1600 °C, 1650 °C and 1700 °C are 31.53 μm, 32.09 μm,

Table 8 Comparison between the calculated and experimental values of the yield strengths (MPa)

T_{sin} (°C)	σ_0	$\Delta\sigma_{ss}$		$\Delta\sigma_{gb}$	$\Delta\sigma_{dis}$	$\Delta\sigma_p$	σ_y	σ_{exp}	Error (%)
		$\Delta\sigma_{sss}$	$\Delta\sigma_{iss}$						
1550	188	908	29	62	401	63	1651	1843	− 10.4
1600			33	61	558	32	1780	2032	− 12.4
1650			36	57	558	48	1795	1995	− 10.0
1700			32	46	349	29	1552	1685	− 7.9

36.76 μm and 57.33 μm, respectively. The corresponding calculated values of $\Delta\sigma_{gb}$ are 62 MPa, 61 MPa, 57 MPa, and 46 MPa, respectively.

The dislocation strengthening effect $\Delta\sigma_{dis}$ is also called deformation strengthening or work hardening. According to the nature of dislocation strengthening, dislocations continue to proliferate after material deformation, and the dislocation density continues to increase, enhancing the interaction between dislocations. In this situation, dislocation slip requires higher stress, making plastic deformation of the material more difficult, and then the strength of the alloy increases. The value of dislocation strengthening $\Delta\sigma_{dis}$ can be expressed as follows:

$$\Delta\sigma_{dis} = M\alpha_T Gb\rho^{1/2}. \tag{23}$$

where M is the Taylor factor. α_T is a constant related to the type of material, ranging from 0.3 to 0.5. In this study, it takes the intermediate value 0.4, G represents the shear modulus, b is the Burgers vector, which is equal to $a/2$, where a is the lattice constant. ρ refers to the dislocation density of the alloy, which can be calculated by referring [40]:

$$\rho = \frac{3E}{G\left(1+2v^2\right)b^2}\varepsilon^2. \tag{24}$$

where E (163.767 GPa) is the elastic modulus, which can be obtained by fitting the four sets of stress–strain datapoints at elastic stage together. v is the Poisson's ratio of the alloy, which can be calculated to be 0.38 by the formula: $G = E/2(1+v)$. ε is the alloy micro strain output from Highscore. For alloy sintered at 1550 °C, 1600 °C, 1650 °C and 1700 °C, ε are 0.23%, 0.32%, 0.32% and 0.2%, and calculated $\Delta\sigma_{dis}$ are 401 MPa, 558 MPa, 558 MPa and 349 MPa, respectively.

The precipitation strengthening effect $\Delta\sigma_{or}$ is also considered when establishing the strength model. A large number of needle-shaped precipitated phases are distributed within the matrix, which hinders the movement of the dislocation. Meanwhile, the uniformly distributed carbides and unknown precipitates formed during MA and SPS can also hinder the movement of dislocations. Due to its low content, however, its contribution is negligible. The precipitation strengthening effect of the needle-shaped precipitated phases can be calculated as follows [41]:

$$\Delta\sigma_p = \frac{0.4MGb\ln\left(\bar{d}/b\right)}{\pi\lambda_p\sqrt{1-v}}. \tag{25}$$

where M is the Taylor factor. G is the shear modulus of the alloy, b refers to the Burgers vector of the matrix phase. Because the precipitated phase in the alloy is needlelike with a large aspect ratio, d and λ_p are used to represent the thickness and spacing of the precipitation similar to needles, respectively. For samples sintered at 1550 °C, 1600 °C, 1650 °C and 1700 °C, the calculated values of $\Delta\sigma_p$ are 63 MPa, 32 MPa, 48 MPa and 29 MPa, respectively.

In summary, the compressive yield strength of $Ti_{62}Nb_{12}Mo_{12}Ta_{12}W_2$ RHEA can be expressed as follows:

$$\sigma_y = 1096 + 69\left(\sqrt{c_m} + b\sqrt{\rho}\right) + \frac{345}{\sqrt{D}} + \frac{69b\ln\left(\frac{\bar{d}}{b}\right)}{\pi\lambda_p\sqrt{1-v}}. \tag{26}$$

The comparison between the calculated strength and the experimental results is listed in Table 8. By calculating the degree of deviation, it can be found that the strength of the alloy can be fairly predicted through this model.

4 Conclusion

The phase formation of the alloy was predicted and $Ti_{62}Nb_{12}Mo_{12}Ta_{12}W_2$ was successfully prepared by MA and SPS. The microstructure is composed of the high-entropy BCC1 phase, titanium-poor BCC2 phase, and the TiC + TiO + TiN composite FCC phase. As the sintering temperature increases, the BCC2 phase gradually dissolves into the BCC1 phase. The density of this alloy is superior to that of some high-temperature alloys and traditional refractory high-entropy alloys. Meanwhile, this alloy has favorable mechanical properties. At room temperature, the yield strength of the alloy sintered at 1600 °C can reach 2032 MPa, and the strain is more than 10%. At 1000 °C, the compressive yield strength of the alloy sintered at 1550 °C is 280 MPa, and no fracture occurs when compressed to 50%. Finally, the alloy strength model was provided and the strengthening mechanism was analyzed. The model shows

fair accuracy with a prediction error ranges from − 7.9% to − 12.4%.

Acknowledgements The authors acknowledge the financial support from the Fundamental Research Program of Shanxi Province (202203021211130), the Innovation and Entrepreneurship Training Program for College Students in Shanxi Province (20220119), the Research Project Supported by Shanxi Scholarship Council of China (2023-068) and the National Natural Science Foundation of China (Grant No. 51801132).

Declarations

Conflict of interest The authors declare that they have no known competing financial interests or personal relationships that could have appeared to influence the work reported in this paper.

References

[1] J.W. Yeh, S.K. Chen, S.J. Lin, J.Y. Gan, T.S. Chin, T.T. Shun, C.H. Tsau, S.Y. Chang, Adv. Eng. Mater. **6**, 5 (2004)
[2] B.S. Murty, J.W. Yeh, S. Ranganathan, *High Entropy Alloys* (Butterworth–Heinemann, Boston, 2014)
[3] S. Ranganathan, Curr. Sci. **85**, 10 (2003)
[4] K.Y. Tsai, M.H. Tsai, J.W. Yeh, Acta Mater. **61**, 13 (2013)
[5] J.W. Yeh, S.Y. Chang, Y.D. Hong, S.K. Chen, S.J. Lin, Mater. Chem. Phys. **103**, 1 (2007)
[6] Y.H. Fang, N. Chen, G.P. Du, M.X. Zhang, J.B. Wu, J. Alloys Compd. **815**, 152486 (2019)
[7] Y.W. Chen, Z.Q. Xu, M. Wang, Y.K. Li, Y. Yang, J. Mater. Sci. Eng. A **792**, 139774 (2020)
[8] D.B. Miracle, O.N. Senkov, J.M. Scott, G.B. Wilks, Intermetallics **19**, 5 (2011)
[9] O.N. Senkov, J.M. Scott, S.V. Senkova, D.B. Miracle, C.F. Woodward, J. Alloys Compd. **59**, 6043 (2011)
[10] Y.D. Wu, Y.H. Cai, T. Wang, J.J. Si, J. Zhu, Y.D. Wang, X.D. Hui, Mater. Lett. **130**, 277 (2014)
[11] V.D. Skibin, N.Y. Yurchenko, A.M. Tikhonovsky, A.G. Salishchev, D.N. Stepanov, J. Alloys Compd. **652**, 266 (2015)
[12] J.S. Han, Dissertation, Lanzhou University of Technology, 2023
[13] B. Kang, J. Lee, H.J. Ryu, S.H. Hong, Mater. Sci. Eng. A **712**, 616 (2018)
[14] Y. Long, X. Liang, K. Su, H. Peng, X. Li, J. Alloys Compd. **780**, 607 (2019)
[15] N. Gao, L.Y. Long, H.Y. Peng, W.H. Zhang, L. Peng, Chin. J. Mater. Res. **33**, 8 (2019)
[16] B. Cantor, I. Chang, P. Knight, Mater. Sci. Eng. A **375–377**, 213 (2004)
[17] Y.Y. Chen, T. Duval, U.D. Hung, J.W. Yeh, H.C. Shih, Curr. Sci. **47**, 2257 (2005)
[18] J.M. Wu, S.J. Lin, J.W. Yeh, S.K. Chen, H.C. Chen, Wear **261**, 513 (2006)
[19] X. Yang, Y. Zhang, P.K. Liaw, Procedia Eng. **36**, 292 (2012)
[20] J.W. Yeh, Eur. J. Control. **31**, 633 (2006)
[21] S.Y. Xing, S.H. Wang, Aluminum and Titanium Alloys (Beijing, 1987)
[22] O.N. Senkov, S.V. Senkova, D.B. Miracle, C. Woodward, Mater. Sci. Eng. A **565**, 51 (2013)
[23] O.N. Senkov, C. Woodward, D.B. Miracle, J. Met. **66**, 10 (2014)
[24] C.C. Juan, M.H. Tsai, C.W. Tsai, C.M. Lin, W.R. Wang, C.C. Yang, S.K. Chen, S.J. Lin, J.W. Yeh, Intermetallics **62**, 76 (2015)
[25] N.D. Stepanov, D.G. Shaysultanov, G.A. Salishchev, M.A. Tikhonovsky, Mater. Lett. **142**, 153 (2015)
[26] H. Chen, A. Kauffmann, S. Laube, I.C. Choi, R. Schwaiger, Y. Huang, K. Lichtenberg, F. Müller, B. Gorr, H.J. Christ, M. Heilmaier, Metall. Mater. Trans. A **49**, 772 (2018)
[27] Y. Long, K. Su, J.F. Zhang, X.B. Liang, H.Y. Peng, X.Z. Li, Materials **11**, 5 (2018)
[28] W.T. Jiang, X.H. Wang, S.Y. Li, T.F. Ma, Y. Wang, D.D. Zhu, Mater. Lett. **328**, 133144 (2022)
[29] B.M. Rice, S.V. Pai, J. Hare, Combust. Flame **118**, 3 (1999)
[30] Y. Zhang, Y.J. Zhou, J.P. Lin, G.L. Chen, P.K. Liaw, Adv. Eng. Mater. **10**, 6 (2008)
[31] A. Takeuchi, A. Inoue, Mater. Trans. **46**, 2817 (2005)
[32] T. Egami, Y. Waseda, J. Non-Cryst. Solids **64**, 113 (1984)
[33] X. Yang, Y. Zhang, Mater. Chem. Phys. **132**, 233 (2012)
[34] S. Guo, C. Ng, J. Lu, C.T. Liu, J. Appl. Phys. **109**, 103505 (2011)
[35] S.S. Lv, Dissertation, Dalian University of Technology, 2022
[36] J.Y. Pan, T. Dai, T. Lu, X.Y. Ni, J.W. Dai, M. Li, Mater. Sci. Eng. **738**, 19 (2018)
[37] W. Wang, L. Yuan, H. Zhang, Z. Wei, H. Zhang, W. Zhang, J. Alloys Compd. **931**, 167558 (2023)
[38] W. Li, D. Xie, D. Li, Y. Zhang, Y. Gao, P.K. Liaw, Prog. Mater. Sci. **118**, 100777 (2021)
[39] Z.C. Cordero, B.E. Knight, C.A. Schuh, Int. Mater. Rev. **61**, 8 (2016)
[40] F. Christien, M.T.F. Telling, K.S. Knight, Scr. Mater. **68**, 506 (2013)
[41] K. Ma, H. Wen, T. Hu, T.D. Topping, J.M. Schoenung, Acta Mater. **62**, 5 (2014)